How to cite: *Angew. Chem. Int. Ed.* **2024**, *63*, e202410747
doi.org/10.1002/anie.202410747

Oxygen Reduction Reaction

Pentagon-Rich Caged Carbon Catalyst for the Oxygen Reduction Reaction in Acidic Electrolytes

*Guoping Chen, Miho Isegawa, Taro Koide, Yasuo Yoshida, Koji Harano, Kenji Hayashida, Shusaku Fujita, Kotaro Takeyasu, Katsuhiko Ariga, and Junji Nakamura**

Abstract: The interaction between electron spin and oxygen molecules in non-platinum catalysts, particularly carbon catalysts, significantly influences the catalytic performance of the oxygen reduction reaction (ORR). A promising approach to developing high-performance catalysts involves introducing five-membered ring structures with spin into graphitic carbons. In this study, we present the successful synthesis of cage-like cubic carbon catalysts enriched with pentagon structures using pentagon ring-containing C_{60} and a NaCl template. The number of pentagons contained in the structure was increased by doping with nitrogen and annealing, and the number of electron spins also increased, thereby improving catalytic activity. The prepared catalyst exhibits remarkable activity in ORR under acidic electrolytes. Furthermore, we elucidate the correlation between the pentagon structure, the number of spin, and catalytic activity, demonstrating that enhanced activity is contingent upon the presence of spin. Density functional theory (DFT) calculations support the role of spin in improving activity. The concept of spin and the introduction of pentagon structures provide new design principles for carbon catalysts.

Introduction

Carbon materials are highly anticipated as electrode catalysts that will be used in large quantities in a carbon-neutral society. In recent years, extensive research has been conducted on carbon catalysts for various electrochemical reactions, including oxygen reduction reactions (ORR) in fuel cells, oxygen evolution reactions (OER), hydrogen evolution reactions (HER) via water electrolysis, and CO_2 reduction reactions (CO_2RR) for chemical conversion of CO_2.[1] The unique properties of carbon catalysts with customized surface features such as elemental doping and defects are highlighted.[2] In particular, nitrogen-doped carbon catalysts for ORR are attracting attention as non-platinum catalysts for fuel cells.[3] However, a major problem with nitrogen-doped carbon catalysts is the deactivation in acidic electrolytes with showing low limiting current in rotating disc experiments of ORR.[4] The deactivation mechanism of nitrogen-doped carbon catalysts in acidic electrolytes has not been fully elucidated. We have proposed that protonation of pyridinic nitrogen (pyridinic N) is the cause of deactivation.[5] It is an important research topic to compare the deactivation mechanism of pyridinic N-doped carbon catalysts with that of nitrogen-free carbon catalysts, such as pentagon-containing carbon catalysts, in acidic electrolytes.

[*] Dr. G. Chen, Prof. Dr. M. Isegawa, Prof. Dr. J. Nakamura
International Institute for Carbon-Neutral Energy Research (I2CNER), Kyushu University
744 Motooka, Nishi-ku, Fukuoka-shi, Fukuoka 819-0395, Japan
E-mail: nakamura.junji.700@m.kyushu-u.ac.jp

Dr. T. Koide
Department of Chemistry and Biochemistry, Graduate School of Engineering, Kyushu University
Moto-oka 744, Nishi-ku, Fukuoka 819-0395, Japan

Prof. Dr. Y. Yoshida
Department of Physics, Kanazawa University,
Kanazawa 920-1192, Japan

Prof. Dr. K. Harano
Center for Basic Research on Materials, National Institute for Materials Science
1-1 Namiki, Tsukuba, Ibaraki 305-0044, Japan

K. Hayashida
Graduate School of Environmental Science, Hokkaido University
Kita 10 Nishi 5, Kita-ku, Sapporo, Hokkaido 001-0010, Japan

K. Hayashida, S. Fujita
Graduate School of Science and Technology, University of Tsukuba
1-1-1 Tennodai, Tsukuba, Ibaraki 305-8573, Japan

Prof. Dr. K. Takeyasu
Institute for Catalysis, Hokkaido University
Kita 21 Nishi 10, Kita-ku, Sapporo, Hokkaido 001-0021, Japan

Prof. Dr. K. Takeyasu
Institute of Pure and Applied Sciences, University of Tsukuba
1-1-1 Tennodai, Tsukuba, Ibaraki 305-8573, Japan

Prof. Dr. K. Ariga
Department of Advanced Materials Science, Graduate School of Frontier Sciences, The University of Tokyo
5-1-5 Kashiwanoha, Kashiwa, Chiba 277-8561, Japan

Prof. Dr. K. Ariga
Research Center for Materials Nanoarchitectonics, National Institute for Materials Science
Namiki 1–1, Tsukuba 305-0044, Japan

Beyond pyridinic N, defects such as pentagons and vacancies have also been reported to create active sites for ORR. These defects can promote charge redistribution on π-conjugated carbon atoms, potentially avoiding the effects of protonation.[5] Especially, Jia et al. demonstrated that edged pentagon defects could serve as primary active sites for acidic ORR, outperforming pyridinic N sites.[5a] However, further studies are needed to understand the catalytic behavior of defects-including carbon catalysts, in which a critical aspect often overlooked in previous studies is the role of electron spin in the defect structure. In ORR catalysis, the interaction of electron spins can significantly influence the energy levels because the activation of the ground state triplet O_2 can be induced by the electrons from the catalyst with high spin concentrations.[6] Furthermore, the concept of singly occupied molecular orbitals (SOMO) becomes crucial in this context.[7] These unpaired electrons are central to facilitating electron transfer processes. For example, Tian et al. shows that σ-type free radical species in graphene belts provide the dominant sites for ORR catalytic activity through the spin-spin interaction.[8] Nonetheless, unlike transition metal-based catalysts, considerably less work has been done to exploit the spin properties in carbon materials with defects since inducing high spin concentrations in carbon matrix systems remains quite challenging. The introduction of pentagon defects has been proposed as a method to induce magnetism, thereby altering spin density and distribution in carbon-based materials.[9] This suggests a promising strategy: creating active carbon sites with spin by integrating a high concentration of pentagon defects.

Selecting an appropriate carbon source is pivotal for introducing pentagon defects into graphitic carbons. Fullerene C_{60} and its derivatives have emerged as promising carbon precursors due to their inherent presence of pentagons that significantly influence electron distribution and spin characteristics. Zhu et al. demonstrated the utilization of intrinsic pentagon defects in C_{60} (PD–C) as an ORR catalyst in alkaline electrolytes.[10] However, limitations exist for PD–C performance in acidic media, highlighting the need for enhanced control over specific surface area and morphology. Furthermore, nitrogen (N) incorporation into C_{60} molecules via amination reactions can be further transformed into pentagon structures under annealing conditions, potentially leading to a high concentration of these active sites.[5a] Moreover, as spherical building blocks, C_{60} and its derivatives facilitate the fabrication of nano- to micro-sized carbon structures with controlled shapes, ranging from well-ordered one-dimensional to three-dimensional forms, by assembly at the molecular level.[11] Particularly promising is the use of templates to prevent agglomeration and tailor surface attributes such as pore distribution, surface area, and overall morphology.[12] Our prior research demonstrated that regulating the growth kinetics of the C_{60} nucleus and employing a droplet template can yield versatile hollow C_{60} spheres.[13] Employing non-carbonizable sodium chloride (NaCl) salt as a template has proven to be an effective, economical strategy to enhance the surface area of carbon precursors. For instance, Zeng et al. observed that a NaCl template significantly improved the surface area of Fe, N, and S tri-doped porous carbon, which exhibited superior activity and stability compared to the Pt/C catalyst for ORR in acidic media.[14] Similarly, we have developed a caged N-doped reduced graphene oxide (Caged-NrGO) catalyst using a NaCl template, which enhanced not only the specific surface area but also the hydrophobicity, thereby boosting its activity for acidic ORR.[15] Given C_{60}'s assembly capabilities, there is potential for constructing cage-like structures using salt templates, harnessing both the high surface area and hydrophobic nature of these configurations to advance the field of carbon-based catalysis.

In this study, by applying a salt-templated approach, cage-like N-doped carbon called Caged-NC, and cage-like carbon without N doping called Caged-C were successfully synthesized with a distinct caged hollow structure and were evaluated for their performance in ORR catalysis. The resulting Caged-NC and Caged-C were processed by annealing engineering to adjust the configuration of the pyridinic N and pentagons. For the Caged-NC, after annealing between 800 and 1100 °C in N_2 atmospheres, activity was observed to increase as doped pyridinic N was removed, and pentagons were generated. The catalyst with higher pentagon concentration exhibits higher magnetism, which could induce singly occupied molecular orbitals and is supposed to contribute to enhanced performance. The results show that the activity has improved further and exhibits outstanding ORR performance in the acidic electrolyte, ascribed to the higher concentration of pentagons. This work manifests the important role of morphology control and helps understand the spin effect of pentagons on ORR performances.

Results and Discussion

The schematic illustrating the salt-templated synthesis strategy is shown in Figure 1a. To endow the catalyst with a caged-like structure, cube-shaped NaCl was chosen as the template for this study. The NaCl aqueous solution was dripped into the acetone solution for recrystallization to obtain the fine NaCl nanocrystal with a size of 500 nm ~4 mm (Figure S1). Here, pristine C_{60} molecules were chosen as the precursor for synthesizing the carbon catalyst without N doping, whereas C_{60}-ethylenediamine (C_{60}-EDA) molecules were used for synthesizing the carbon catalyst with N doping. Regarding C_{60}-EDA molecules, the pristine C_{60} molecules can be dissolved in EDA solvent by chemical reaction to form a crosslinked structure to generate C_{60}-EDA nuclei. The chemical equation is shown in Figure S2. Photographs of the C_{60}-EDA solution and dried C_{60}-EDA powder, and the Fourier transform infrared (FTIR) spectrum of the C_{60}-EDA powder are shown in Figures S3a and S3b, respectively. These results indicate that the C_{60}-EDA complex was formed, as previously reported.[13,16] For the synthesis of cage-like N-doped carbon (Caged-NC), first, the NaCl nanocrystal was mixed with C_{60}-EDA solution so that C_{60}-EDA molecules would attach to the surface of the NaCl nanocrystal and stack one by one to form a cube structure. The obtained powder, after drying, was annealed at 750 °C at N_2 atmospheres. Throughout the pyrolysis process, the

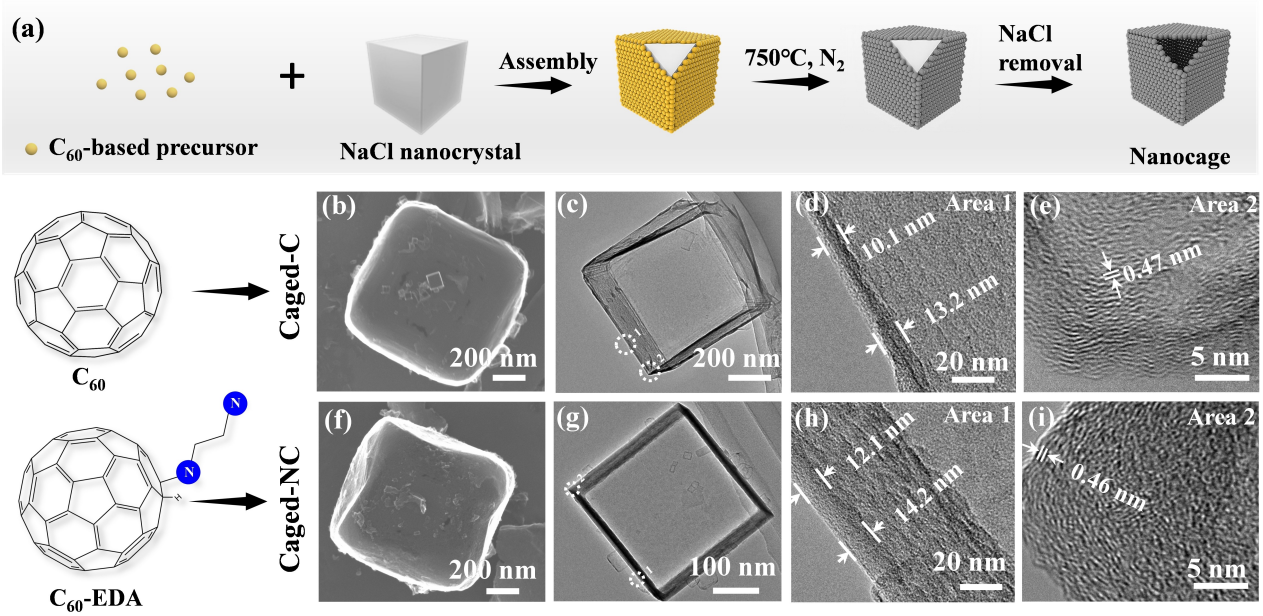

Figure 1. (a) The schematic illustrating the salt-templated synthesis of nanocages from C_{60}-based precursor. Pristine C_{60} molecules were employed for synthesizing the carbon catalyst without N doping (Caged-C), while C_{60}-ethylenediamine (C_{60}-EDA) molecules were used for synthesizing the carbon catalyst with N doping (Caged-NC). Electron microscope imaging for Caged-C (b-e) and Caged-NC (f-i): SEM images of Caged-C (b) and Caged-NC (f); TEM images of Caged-C (c) and Caged-NC (g); (d) high-resolution TEM image in area 1 shown in (c) that indicates the thickness of the Caged-C; (e) high-resolution TEM image in area 2 shown in (c) that indicates the fringe spacing of Caged-C; (h) high-resolution TEM image in area 1 shown in (g) that indicates the thickness of the Caged-NC; (i) high-resolution TEM image in area 2 shown in (g) that indicates the fringe spacing of Caged-NC.

NaCl nanocrystal acted as a cube template, preventing the collapse and agglomeration of the C_{60}-EDA assembly and maintaining the cube structure. Simultaneously, N elements, originating from the decomposition of ethylenediamine and amines functionalized C_{60}-EDA, were doped into the C_{60} fragments..[17] Finally, water was employed to remove the NaCl, resulting in the formation of caged-like N-doped carbon (Caged-NC). On the other hand, for the synthesis of cage-like carbon (Caged-C), pristine C_{60} molecules were dissolved in a p-xylene solvent and underwent a similar synthesis procedure to that of Caged-NC.

Figure 1b-i shows the SEM and TEM images of the resulting Caged-C and Caged-NC. Both samples present their caged structures under the synthesis assisted by the NaCl template. The morphology and size of the cavities are similar to NaCl nanocrystals (Figure S1e–g), suggesting that NaCl has successfully acted as a template to induce the caged structure in the materials. TEM images (Figure 1c, g) further indicate that the cavity exists in the Caged-C and Caged-NC samples. N-doped carbon (NC) was produced with a similar procedure to demonstrate the role of NaCl templates, where the C_{60}-EDA molecules as the precursor but assembled without NaCl templates. Figure S4 shows that NC exhibits a solid three-dimensional cross-linked morphology, indicating the aggregation of C_{60}-EDA. High-resolution TEM images (Figure 1d, h) in the specific area indicate the thickness of the Caged-C/Caged-NC is approximately 10–14 nm. Besides, Figure 1e and Figure 1i suggest an amorphous carbon structure of both samples after annealing at 750 °C. It is worth mentioning that both Caged-C and Caged-NC exhibit distinctive short, curved fringe in the cage's corner that appears to have no orientation relative to each other. The curved fringe is distinct from the flat graphene structure and could be a result of the utilization of C_{60}-based molecules as building units. These structures comprise a stack of 20–30 layers with the interplanar distance ranging from 0.46 to 0.47 nm, thus being larger than the typical plane distance in graphite (0.34 nm).[18] Such a short, curved structure would be expected to introduce more edged and defective carbon, therefore benefiting an exceptionally high surface area and catalyst activities.[19]

Table 1 summarizes the surface area, pore volume, and N contents of Caged-C and Caged-NC. The N-doping content calculated from X-ray photoelectron spectroscopy (XPS, Figure S5a) for Caged-C, NC (Table S1) and Caged-NC is 0, 1.09, and 1.07 at%, respectively. Since the synthesis of Caged-C did not utilize any N source, the detected N content is zero. Additionally, NC and Caged-NC result in similar N content and N constitute. Four types of N species

Table 1: Surface area, pore volume, and N contents of Caged-C and Caged-NC.

	Surface area ($m^2 g^{-1}$)	Pore volume ($cm^3 g^{-1}$)	Total N (at%)	Pyridinic N (at%)	Graphitic N (at%)	Pyrrolic N (at%)	Oxidized N (at%)
Caged-C	606.624	1.399	–	–	–	–	–
Caged-NC	812.738	1.087	1.07	0.37	0.34	0.12	0.24

can be identified from the N 1s spectrum: pyridinic N (~398.2 eV), pyrrolic N (~399.6 eV), graphitic N (~400.8 eV), and oxidized N (~403.2 eV).[20] Figure S5b shows the X-ray diffraction (XRD) pattern of NC, Caged-C, and Caged-NC. Compared to pristine C_{60}, the characteristic peaks of C_{60} have disappeared in all samples, indicating that the molecular structure of C_{60} has been cracked after annealing, leading to the formation of C_{60} fragments. The broad peak observed around 25 degrees represents the generation of amorphous graphite.[21] The N_2 adsorption/desorption isotherms and the pore width distribution curves of NC, Caged-C, and Caged-NC are shown in Figure S5c, d. As listed in Table 1, and Table S1, compared to NC, the introduction of the cavity structure significantly increases the specific surface areas and pore volumes of the Caged-C, and Caged-NC. In particular, the surface area/pore volumes of Caged-NC is 812.74 $m^2 g^{-1}$/1.087 $cm^3 g^{-1}$. As shown in Figure S5d, all the sample possess similar hierarchical distributions of micropores and mesopores. The micropores are mainly distributed in 1.4 nm and 1.8 nm. Caged-NC contains a larger quantity of micropores than NC and Caged-C. Therefore, it can be concluded that the utilization of the NaCl template and ethylenediamine has an important impact on the formation of micropores.

Based on the above discussion, it was shown that, apart from the absence of N, Caged-C exhibits similar morphology and fragmented C_{60} structures to Caged-NC, which facilitates a comparative investigation of the impact of pyridinic N and pentagons on ORR activity. Hence, a series of annealing experiments were conducted on Caged-NC and Caged-C to adjust the pentagon configuration. The samples were subjected to annealing at high temperatures of 800 °C, 900 °C, 1000 °C, and 1100 °C under a N_2 atmosphere. As shown in Figure S6, the samples maintain their caged structure even after annealing at 1100 °C. Figure S7 indicates that the samples do not ultimately form crystalline graphite at 1100 °C. Instead, they largely retain an amorphous structure. Moreover, Fast Fourier transform (FFT, Figure S7e, f) patterns revealed the absence of a periodic pattern, with only amorphous halo features observed. This observation suggests that the carbon networks comprise not only hexagons but also pentagons or other types of defects.[22]

The configuration of pyridinic N and pentagon is examined using Raman spectroscopy (Figure 2a, b) and XPS experiments (Figure 2c). As shown in the Raman spectra, all samples displayed two broad peaks at around 1345.5 cm^{-1} and 1591.5 cm^{-1}, respectively.[23] Raman spectra are sensitive to carbon structure, the results are fitted into five bands (G, D1, D2, D3, and D4) at the range of 800–2000 cm^{-1} (Table S2).[24] It has been reported that the appearance of the D3 peak around 1500 cm^{-1} in Raman spectra signifies disorder in the graphite lattice, often due to the inclusion of pentagons and other non-hexagonal rings.[25] Meanwhile, in our study, we used C_{60} as the starting material. The C_{60} molecule consists of 12 pentagon rings and 20 hexagon rings.

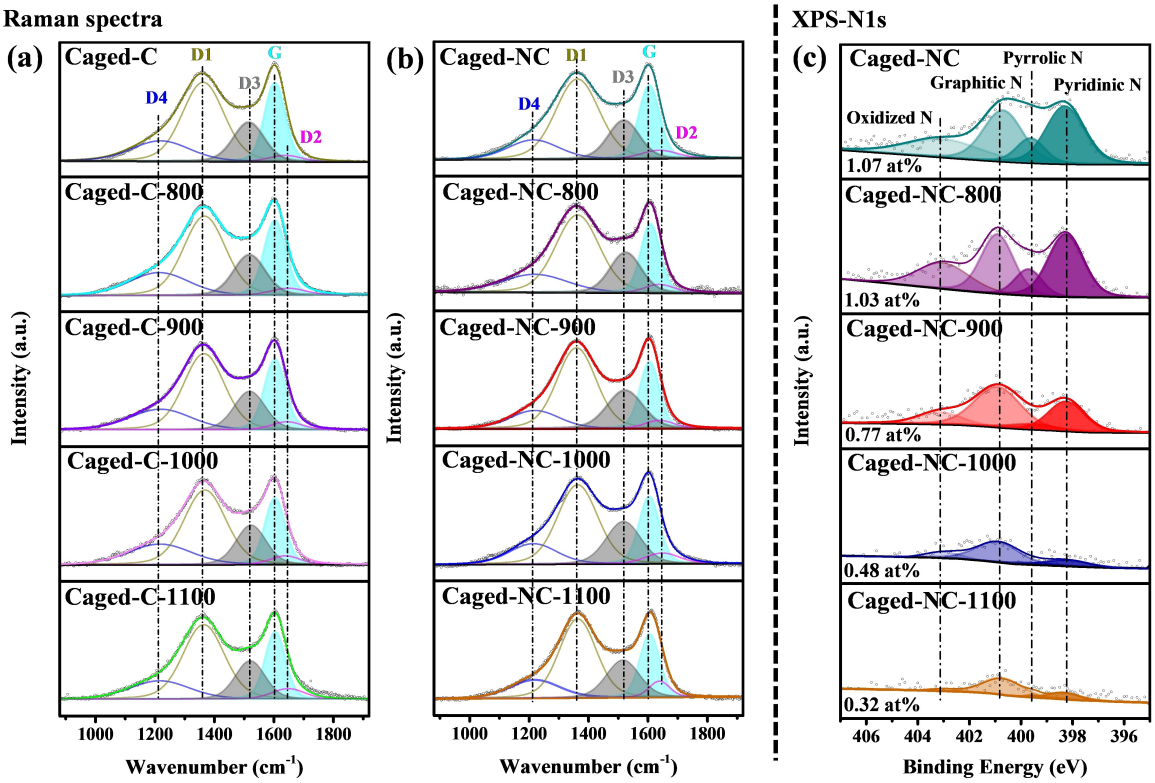

Figure 2. Raman spectra of Caged-C and its pyrolysis derivatives (a) and Caged-NC and its pyrolysis derivatives (b). (c) XPS spectra of Caged-NC and its pyrolysis derivatives. The 800, 900, 1000, and 1100 indicate anneal of the samples at 800, 900, 1000, and 1100 °C at N_2 atmospheres, respectively.

When C_{60} aggregates are annealed at 700 °C or higher, graphitization occurs, but it is expected that the pentagonal structure remains. It is also known that the pentagonal structure is transformed by the removal of doped pyridinic N in graphitic carbons. In this study, the presence of the pentagonal structure and the resulting disorder were confirmed by high-resolution TEM imaging. It is thus considered that the presence of the pentagonal structure may be reflected in the intensity of the D3 peak. Hence, in the present study, we adopt the D3 peak as an indicator of the pentagon structure.[24b,26] It is a commonly observed phenomenon that the intensity of the D3/G peak increases as the annealing temperature rises from 800 °C to 1000 °C for both Caged-C and Caged-NC samples. However, at 1100 °C, the intensity of the peak decreases. This trend can be explained by the fact that pentagons are incorporated into the graphite layer between 800 °C and 1000 °C. However, at a higher temperature of 1100 °C, some of the thermodynamically unstable pentagonal ring structures are graphitized and converted to hexagons. The D3/G peak intensity of the Caged-NC series is greater than that of the Caged-C series. In addition, the difference between the Caged-C and Caged-NC samples can be attributed to the process of pentagon formation by nitrogen removal, which occurs actively around 800–1000 °C. It has previously been demonstrated that the high-temperature heat treatment of pyridinic N results in the formation of pentagons.[5a,27] Figure 2c shows the XPS N1s spectra of Caged-NC and its pyrolysis derivatives Caged-NC-800, 900, 1000, and 1100. The N contents derivatives from XPS results are listed in Table S3. Due to the stable graphitic N configuration in carbonation, graphitic N contents are almost similar from Caged-NC (0.34 at%) to Caged-NC-800 (0.32 at%), Caged-NC-900 (0.39 at%), Caged-NC-1000 (0.29 at%) and Caged-NC-1100 (0.21 at%). Nevertheless, the pyridinic N concentrations decrease obviously from 0.36 at% in Caged-NC-800 to 0.06 at% in Caged-NC-1100 with the rising of pyrolysis temperature. Based on Raman and XPS results, for the samples of Caged-NC and its pyrolysis derivatives, the increase in the pentagon's percentage during the pyrolysis process should be ascribed to the removal of pyridinic N dopants.[5a,27b, 28]

Figures 3a and 3b depict the linear sweep voltammetry (LSV) curves of the Caged-C and Caged-NC catalysts, along with their pyrolysis derivatives, for ORR in 0.1 M H_2SO_4 at a rotation rate of 1600 rpm. To illustrate the role of the NaCl template, the activity of catalyst NC was also measured and shown in Figure S8. The onset potential (E_{onset}) at 0.1 mA cm^{-2} for NC, Caged-C, and Caged-NC catalysts were 0.53, 0.42, and 0.71 V (vs. RHE), and the half-wave potentials ($E_{1/2}$) were 0.32, 0.14, and 0.43 V (vs. RHE), respectively. First, it should be pointed out that the $E_{1/2}$ for Caged-NC compared to NC was with an enhancement of 0.11 V, which suggests that the caged structure due to the salt-templated method increases the activity. Additionally, due to the involvement of the N doping, an increased activity of the Caged-NC catalyst compared to Caged-C was observed.[29] While the higher activity of Caged-NC compared to Caged-C could be attributed to the active site of

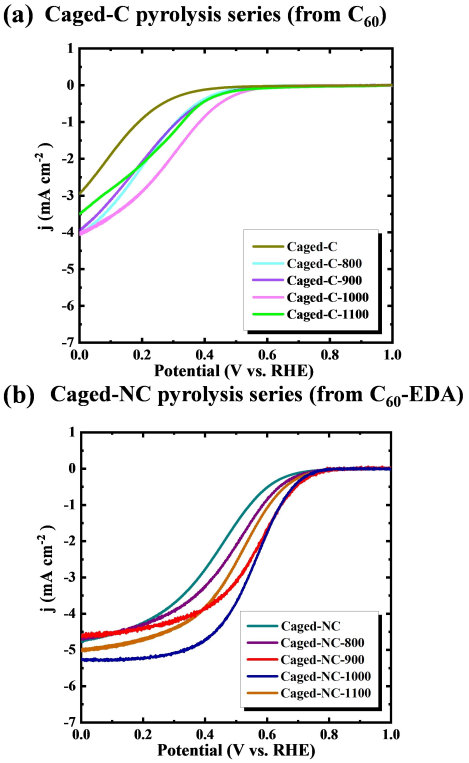

Figure 3. LSV curves of Caged-C and its pyrolysis derivatives (a), and Caged-NC and its pyrolysis derivatives (b) in O_2-saturated conditions in 0.1 M H_2SO_4 electrolyte recorded at a rotation rate of 1600 rpm.

pyridinic N, it is worth noting that the inherent pentagons in C_{60} are also considered as one of the active sites of ORR.[5a,30] The relatively poor catalytic activity of Caged-C may be attributed to the lower concentration of pentagonal active sites. Besides, the introduction of N is conducive to the formation of pentagons during the pyrolysis process, further contributing to the enhanced activity of Caged-NC compared to Caged-C. With further analysis, in the Caged-C catalyst series (Figure 3a), the $E_{1/2}$ values (vs. RHE) for the 800, 900, 1000, and 1100 catalysts were 0.21, 0.21, 0.29, and 0.25 V, respectively. Conversely, in the Caged-NC catalyst series (Figure 3b), the $E_{1/2}$ values for the 800, 900, 1000, and 1100 catalysts were 0.48, 0.56, 0.56, and 0.49 V, respectively. It can be seen that both catalyst series exhibited similar temperature dependencies. Specifically, within the pyrolysis temperature range of 800–1000 °C, the performance of catalysts from both series improved with increasing temperature. Therefore, the increased activity of samples from 800–1000 °C can be attributed to the structure formed during the pyrolysis process. Besides, the limiting current value for the Caged-NC catalyst series is close to 5 mA cm^{-1} (comparable to Pt/C catalyst), and the Caged-NC-1000 demonstrates a 4e$^-$ transfer process (Figure S9) with calculated n values at 0.3 V vs. RHE of ~3.75, suggesting the protonation of pyridinic N issue toward the ORR in acidic conditions was effectively suppressed. Such remarkable limiting current, in comparison to other N-doped carbon catalysts reported in the previous literature,[31] should be attributed to the

presence of the additional non-pyridinic N active site. This is also consistent with the XPS analysis. It was observed that the activity of the Caged-NC catalysts within the pyrolysis temperature range of 800–1000 °C increased as the pyridinic N content decreased (Figure 2c), though pyridinic N is widely recognized as an active site for ORR. We also investigated the effect of different electrolytes on the ORR activity and durability of the Caged-NC-1000 catalyst. As shown in Figure S10, there was no significant difference in the onset potentials of the ORR under both 0.1 M·$HClO_4$ and 0.1 M·H_2SO_4. This means that the acidic conditions themselves do not have a major impact on the catalytic activity of ORR. However, a slight difference in the behavior was observed, suggesting a difference in proton conductivity. Besides, the durability was found to be high. As shown in Figure S11, the $E_{1/2}$ was found to decrease within 0.04 volts after 200 cycles of cyclic voltammetry (CV) from 1 V to 0 V vs. RHE in oxygen-saturated 0.1 M H_2SO_4 at room temperature, indicating the high durability of the catalyst.

We proceeded with catalyst analysis assuming that the additional active site includes the pentagon structure with spin. Figure 4a–c shows the correlation of pyridinic N, graphitic N, and pentagon concentration of catalysts with the activities, respectively. Figure 4a depicts the correlation between pyridinic N and the $E_{1/2}$, which indicates that the activity of the Caged-NC catalysts within the pyrolysis temperature range of 800–1000 °C increased as the pyridinic N content decreased as discussed before. Figure 4b depicts the correlation between graphitic N and the $E_{1/2}$ and no discernible correlations were observed. The relative intensity of the D3 band (I_{D3}/I_G) was proposed as a means to characterize the concentrations of pentagons in the catalysts.[26a,32] Hence, the correlation between the pentagon concentration (D3/G area ratio) and catalytic activity was also evaluated (Figure 4c). As shown in Figure 4c, the blue solid line and black solid line represent the fitting lines of the Caged-C series and Caged-NC series, respectively. It is found that the D3/G area ratio is highly correlated to $E_{1/2}$ with Pearson correlation coefficient values of 0.98 and 0.97 for the Caged-C series and Caged-NC series, respectively. Besides, E_{onset} is also linearly related to D3/G area ratios with Pearson correlation coefficient values of 0.90 and 0.91 for the Caged-C series and the Caged-NC series, respectively (Figure S12a). Notably, both series exhibited a similar trend, wherein an increase in pentagon concentration corresponded to enhanced activity, indicating that the presence of additional pentagon defects contributes to the boost in catalytic activity. Additionally, owing to the involvement of N elements, the Caged-NC 800, 900, 1000, and 1100 displayed heightened catalytic activity even at lower D3/G values, surpassing the activity levels of the Caged-C series within the same D3/G ranges. The blue dashed line, extending as a visual extension from the blue fitted line of the Caged-C series, provides an expected correlation between the concentration of pentagons and the corresponding activity level in a theoretical context. It is noteworthy that the blue dashed line is anticipated to intersect with the black fitted line at approximately D3/G = 1.1. This value is considered as an N absent state for the Caged-NC series, affirming the correctness of the theoretical correlation depicted by the dashed line. Although the current data indicates that activity improves with an increasing D3/G ratio, further investigation is required to ascertain whether catalytic performance increases at higher D3/G values. In particular, it is necessary to ascertain

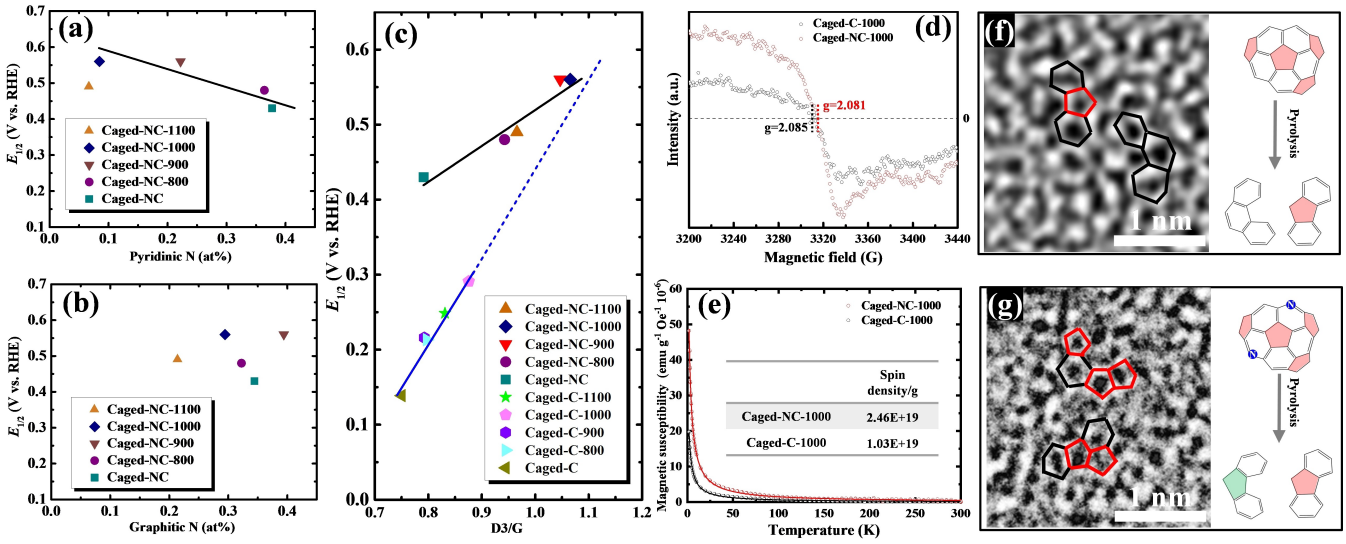

Figure 4. The correlation of pyridinic N, graphitic N, and pentagon concentration of catalysts with the activities, respectively: (a) $E_{1/2}$ vs. pyridinic N ratio and (b) $E_{1/2}$ vs. graphitic N ratio. (c) Correlation of $E_{1/2}$ and D3/G ratio of Caged-C, Caged-NC, and their pyrolysis derivatives. The blue dashed line extending from the blue fitted line represents the theoretical correlation between the concentration of pentagons and activity. ESR spectra (d) and magnetic susceptibility measurement (e) of Caged-C-1000 and Caged-NC-1000. The Aberration-corrected TEM images for Caged-C-1100 (f) and Caged-NC-1100 (g), where the schematic illustrates the pyrolysis process of C_{60} fragments and N-doped C_{60} fragments, respectively. The 800, 900, 1000, and 1100 indicate anneal of the samples at 800, 900, 1000, and 1100 °C at N_2 atmospheres, respectively.

whether there are any changes in catalytic activity depending on the location of the pentagonal ring. A correlation analysis between the $E_{1/2}$ and other factors, including G peak intensity (Figure S12b), D1/G ratio (Figure S12c), D2/G ratio (Figure S12d), and D4/G ratio (Figure S12e), was conducted based on the Raman fitting results. However, no discernible correlation between the $E_{1/2}$ and these factors was observed at the current stage. We also discussed the effect of electrical conductivity and surface area on the change in ORR activity due to annealing temperature. As shown in Figures S13 and S14, impedance measurements showed no significant change in electrical conductivity due to annealing and the conductivity was large enough to have negligible effect on LSV. Regarding the correlation between surface area and ORR activity, the cubic structure does not change even after annealing at 1100 °C (Figure S6) in this study, and the surface area does not change significantly as expected (Figure S15). However, the ORR activity changed depending on the annealing temperature (Figure 3), which is thought to be due to the dependence of ORR activity on the number of spin. We are currently investigating the relationship between the annealing temperature and the number of spin.

High-concentration pentagon could lead to unique spin configurations, further impacting the material's catalytic abilities and electronic properties. Magnetic measurements are crucial for comprehending spin-related properties. To mitigate the potential impact of N elements on the measurements, Caged-NC-1000, with a pyridinic N content of only 0.08 at%, was selected as the measurement specimen. A comparative analysis was undertaken with Caged-C-1000 to explore the influence of pentagon concentration on spin properties. In Figure 4d, the electron spin resonance (ESR) spectra, recorded under atmospheric conditions, reveal broadening signals in both the Caged-C-1000 and Caged-NC-1000 samples, indicating the presence of spins. Such broadening signals typically arise when radicals are not uniformly distributed in the bulk. The g-value for a free electron is 2.00232, and deviations from this value, as observed in our spectra, are attributed to magnetic interactions and the environment.[33] Notably, the observed broad peak around $g = 2.08$ in the ESR measurement is attributed to the adsorption of O_2, which occupies the sample's spin site, causing a shift and broadening of the peak.[34] Figure 4e presents the temperature dependence of the magnetic susceptibilities of the Caged-C-1000 and Caged-NC-1000 measured at 1000 Oe in the temperature range between 1.8 and 300 K. Before measurement, the samples underwent six cycles of vacuuming to eliminate O_2 from the air and were subsequently measured under a helium atmosphere. As we will describe later, the data are after the subtraction of temperature-independent terms. Both samples show typical Curie-like behaviors indicating the existence of paramagnetic moments.[35] The motion of electrons around double bonds which are adjacent to the vertices of pentagons is identified to be responsible for the paramagnetic term.[36] We have fit magnetic susceptibility χ to a modified Curie–Weiss law:[34b]

$$\chi = \frac{C}{T - \theta} + \chi_0$$

where C is the Curie constant, θ is the Weiss temperature, and χ_0 represents temperature-independent contributions. We have calculated the magnitude of spin number N using the following equation:[34b]

$$N = \frac{3Ck_B}{g^2\mu_B{}^2 S(S+1)}$$

where S is the spin value, μ_B is the Bohr magneton, g is the electron g-value and k_B is the Boltzmann constant. Assuming $g = 2$ and $S = 1/2$ is expected for unpaired electrons due to dangling bonds of disordered carbons. The magnitude N for the Caged-NC-1000 sample is $2.46E+19\ g^{-1}$, surpassing that of Caged-C-1000 ($1.03E+19\ g^{-1}$). It is evident that the augmentation in pentagon formation due to N removal contributes to the elevated magnetization observed in the Caged-NC-1000 sample.[37]

The aberration-corrected TEM images of Caged-C-1100 (Figure 4f) and Caged-NC-1100 (Figure 4g) provide insights into the structural differences between the carbon materials. Caged-C-1100 maintains a clear carbon framework with inherent pentagon shapes derived from the C_{60} fragment.[38] In contrast, Caged-NC-1100 showcases coupled pentagons, transforming during pyrolysis due to nitrogen doping, leading to pentagon defects. The N doping appears critical for creating a high density of active pentagon sites[39] The electrocatalytic performance of Caged-C series derivatives in acidic ORR environments is underwhelming, likely due to a scarcity of active pentagon sites. The enhanced activity of the Caged-NC series is attributed to an increase in the number of pentagon-shaped reactive sites. The higher density of the pentagon is believed to enhance the spin density, emphasizing the crucial role of spin-structure interactions in electrocatalytic processes.

We performed DFT calculations for free energy changes during O_2 adsorption and reduction processes (Figure 5a), molecular orbital diagram including both alpha and beta spin orbitals (Figure 5b), and spin properties in pentagon-containing aromatics and nitrogen-containing aromatics (Figure 5c) to elucidate the electrochemical reduction process and the correlation between spin density and oxygen adsorption. Four model molecules were studied: frag-1 is a molecule consisting only of hexagons (phenanthrene), frag-2 is a molecule with a pentagon, frag-N-1 is a molecule with an NH group, and frag-N-2 is a molecule with an NH group and a pentagon. Note that frag-N-1 and frag-N-2 are pyridinic N (pyri-N) containing molecules and a proton is added to pyri-N in consideration of acidic conditions so that the initial state of nitrogen in frag-N-1 and frag-N-2 is pyri-NH^+. Upon electron reduction, pyri-NH^+ changes to pyri-NH. We have reported that the formation of pyri-NH is an important catalytic function of pyri-N in the O_2 adsorption process. That is, the electrons added in the reduction of pyri-NH^+ to pyri-NH singly occupy the π^* orbital, and pyri-NH becomes an open-shell system with spin density.[40] The

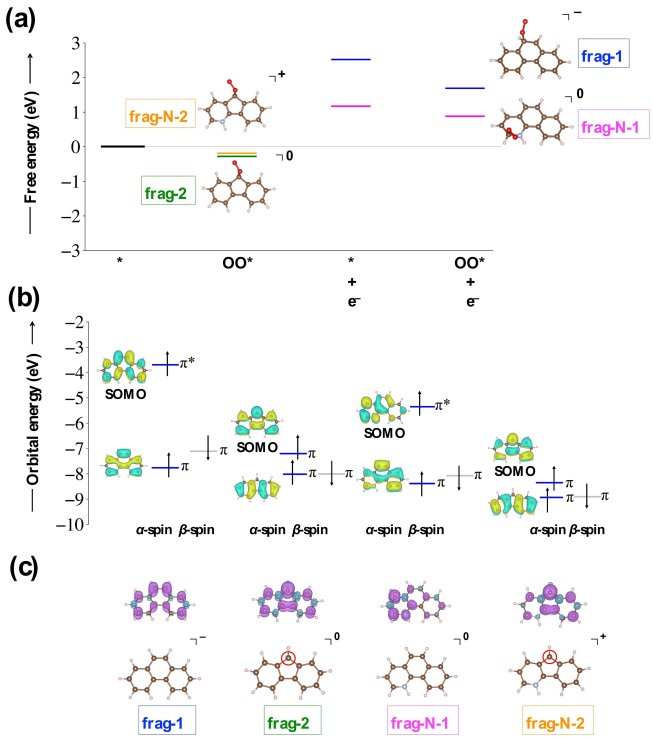

Figure 5. (a) Free energy profiles of electron reduction and O_2 adsorption processes for four fragment models: phenanthrene(frag-1), a molecule with a pentagon (frag-2), a molecule with an NH-group (frag-N-1), a molecule with an NH group and a pentagon (frag-N-2). (b) Molecular orbital diagram including both alpha and beta spin orbitals. (c) Charge state and spin density distributions for four fragment models. The red circles indicate the atomic sites of maximum spin density in the molecules containing the pentagon.

generated spin density then induces interaction with O_2 and adsorption becomes possible. In this calculation, we thus investigated the relationship between the spin behavior and O_2 adsorption in frag-N-1 containing pyri-NH, frag-2 containing pentagon, frag-N-2 containing both, and frag-1 containing neither.

Figure 5a shows the DFT results of O_2 adsorption processes for four model molecules. First, O_2 was not adsorbed to the hexagon-only molecule frag-1 and the pyri-NH^+ containing molecule frag-N-1 without electron reduction so the results are not shown in this step of O_2 adsorption. However, O_2 was adsorbed on pentagon-containing molecules frag-2 and frag-N-2 without reduction. The adsorption energy was similar as −0.28, and −0.19 eV for frag-2 and frag-N-2, respectively, indicating that the effect of pyri-NH^+ is not large. On the other hand, in molecules without a pentagon, O_2 was adsorbed only when they were reduced as shown by blue and pink lines. The energy differences between before and after O_2 adsorption correspond to the O_2 adsorption energy. These results indicate that the pentagon plays a significant role in the adsorption of O_2 and that O_2 is adsorbed even without the reduction of pentagon-containing molecules.

The atom labels for carbon atoms in the four fragment models are shown in Figure S16 and the corresponding O_2 binding energies of each carbon atom for different redox states of fragment models are listed in Table S4. Figure 5a also shows the sites where O_2 is most strongly adsorbed. As shown in Figure 5a, for molecules containing pentagon (frag-2 and frag-N-2), O_2 is adsorbed on the vertices carbon site of the pentagon ring. The O_2-absorbed carbon atom is not shared with the adjacent hexagon ring. Since the present experimental results suggested that spin is related to ORR activity, it is expected that the spin is localized on this carbon atom in the pentagon, which is responsible for the adsorption of O_2 as the initial process of ORR. We thus investigated the spin properties of the four molecules using DFT calculations. As a result, it turns out clearly that the spin properties are completely different depending on whether there is a pentagon ring or not. As shown in Figure 5b, for frag-1, and frag-N-1 without pentagons, the SOMO is characterized by π* orbitals and is energetically high. Furthermore, it can be seen from the density distribution of spin (Figure 5c) that the spin for frag-1, and frag-N-1 are delocalized to each atom, exhibiting relatively lower spin density of each atom site. The delocalization can be explained by the character of the π* orbital. On the other hand, in frag-2 and frag-N-2, SOMO is lower in energy in the π orbital. The spin density is highly localized on the vertices carbon atom of the pentagon (red circled carbon atom in Figure 5c), which is not shared with the adjacent hexagon ring and shows higher density than other carbon atoms. Note that there is also a spin density on the opposite carbon due to the conjugation of the p_z orbital in the pentagon. The present DFT results clearly indicate that the spin density localized on the pentagon enables O_2 adsorption. Based on the experimental results and DFT results, we concluded that the origin of the ORR activity of the pentagon-containing carbon catalyst lies in the spin that inherently exists in the pentagon ring. Although the full mechanism of ORR in pentagon-containing carbon catalysts has not yet been elucidated, the free energy profile calculated assuming a four-electron mechanism (Figure S17) shows an overall downhill, suggesting that ORR does occur. The computational results are based on a rather simplified model system to see the effect of the introduction of the pentagon and therefore will remain a qualitative discussion. The main message of this study is that the localized spin density of the pentagon plays an important role in the adsorption of O_2, an initial step in the ORR. The experimental and DFT results strongly suggest that one of the key factors in the ORR activity of pentagon-containing carbon catalysts is the localized spin density of the pentagon, which is inherently present in the pentagonal ring.

Conclusion

Our study demonstrates the synthesis of Caged-C and Caged-NC catalysts using a NaCl salt template, a conducive method to creating C_{60}-derived catalysts with distinct caged structures and a high density of pentagon active sites. Compared to Caged-C, the Caged-NC catalysts with N doping, subjected to N_2 annealing at temperatures between

800 to 1100 °C, exhibited a notable increase in ORR activity. This annealing process facilitated the formation of additional pentagon defects, affecting the spin properties of the material, and potentially enhancing electrochemical performance. The Caged-NC-1000 catalyst, demonstrated excellent ORR performance in acidic media, marked by a high onset potential of 0.76 V vs. RHE and a pronounced diffusion-limited region, indicative of facilitated electron transfer. DFT calculations supported the role of spin in enabling O_2 adsorption for enhancing activity. This research highlights the importance of pentagon with electron spin in designing efficient carbon-based catalysts for ORR, offering new principles for catalyst development.

Supporting Information

The authors have cited additional references within the Supporting Information.[41]

Acknowledgements

This work was supported by a JSPS Grant-in-Aid for Scientific Research (KAKENHI) Grant Number JP23H05459 and JP23H04874. The authors would like to express their gratitude to Mr. Shuhei Shimoda at the Institute for Catalysis, Hokkaido University for conducting the BET measurements on commission. The authors also appreciate the support from the Joint Usage/Research Center for Catalysis.

Conflict of Interest

The authors declare no conflict of interest.

Data Availability Statement

The data that support the findings of this study are available on request from the corresponding author. The data are not publicly available due to privacy or ethical restrictions.

Keywords: Carbon catalyst · Oxygen reduction reaction · O_2 absorption · Pentagon · Spin

[1] a) X. Duan, J. Xu, Z. Wei, J. Ma, S. Guo, S. Wang, H. Liu, S. Dou, *Adv. Mater.* **2017**, *29*, 1701784; b) G. A. Ferrero, A. B. Fuertes, M. Sevilla, M.-M. Titirici, *Carbon* **2016**, *106*, 179–187; c) S. K. Singh, K. Takeyasu, J. Nakamura, *Adv. Mater.* **2019**, *31*, 1804297; d) H. Wang, T. Maiyalagan, X. Wang, *ACS Catal.* **2012**, *2*, 781–794.

[2] L. H. Zhang, Y. Shi, Y. Wang, N. R. Shiju, *Adv. Sci.* **2020**, *7*, 1902126.

[3] a) X. Feng, Y. Bai, M. Liu, Y. Li, H. Yang, X. Wang, C. Wu, *Energy Environ. Sci.* **2021**, *14*, 2036–2089; b) L. Zhang, L. Li, H. Chen, Z. Wei, *Chem. Eur. J.* **2020**, *26*, 3973–3990.

[4] a) K. Gong, F. Du, Z. Xia, M. Durstock, L. Dai, *Science* **2009**, *323*, 760–764; b) Y. Zhang, K. Fugane, T. Mori, L. Niu, J. Ye, *J. Mater. Chem.* **2012**, *22*, 6575–6580; c) J. Liang, Y. Jiao, M. Jaroniec, S. Z. Qiao, *Angew. Chem. Int. Ed.* **2012**, *124*, 11808–11808.

[5] a) Y. Jia, L. Zhang, L. Zhuang, H. Liu, X. Yan, X. Wang, J. Liu, J. Wang, Y. Zheng, Z. Xiao, *Nat. Catal.* **2019**, *2*, 688–695; b) P. Jiang, K. Jiang, D. Tranca, J. Zhu, F. Qiu, C. Ke, C. Lu, E. Kymakis, X. Zhuang, *Adv. Mater. Interfaces* **2021**, *8*, 2100051.

[6] G. Yang, J. Zhu, P. Yuan, Y. Hu, G. Qu, B.-A. Lu, X. Xue, H. Yin, W. Cheng, J. Cheng, *Nat. Commun.* **2021**, *12*, 1734.

[7] L. Lin, P. Su, Y. Han, Y. Xu, Q. Ni, X. Zhang, P. Xiong, Z. Sun, G. Sun, X. Chen, *eScience* **2024**, 100264.

[8] Y. Tian, H. Cao, H. Yang, W. Yao, J. Wang, Z. Qiao, A. K. Cheetham, *Angew. Chem. Int. Ed.* **2023**, *62*, e202215295.

[9] K. N. Anindya, A. Rochefort, *J. Phys. Chem. C* **2023**, *127*, 22856–22864.

[10] J. Zhu, Y. Huang, W. Mei, C. Zhao, C. Zhang, J. Zhang, I. S. Amiinu, S. Mu, *Angew. Chem. Int. Ed.* **2019**, *58*, 3859–3864.

[11] a) N. Furuuchi, R. G. Shrestha, Y. Yamashita, T. Hirao, K. Ariga, L. K. Shrestha, *Sensors* **2019**, *19*, 267; b) M. R. Benzigar, S. Joseph, H. Ilbeygi, D. H. Park, S. Sarkar, G. Chandra, S. Umapathy, S. Srinivasan, S. N. Talapaneni, A. Vinu, *Angew. Chem. Int. Ed.* **2018**, *130*, 578–582.

[12] K. Elumeeva, N. Fechler, T.-P. Fellinger, M. Antonietti, *Mater. Horiz.* **2014**, *1*, 588–594.

[13] G. Chen, F. Sciortino, K. Takeyasu, J. Nakamura, J. P. Hill, L. K. Shrestha, K. Ariga, *Chem. Asian J.* **2022**, *17*, e202200756.

[14] H. Zeng, W. Wang, J. Li, J. Luo, S. Chen, *ACS Appl. Mater. Interfaces* **2018**, *10*, 8721–8729.

[15] S. K. Singh, K. Takeyasu, K. Homma, S. Ito, T. Morinaga, Y. Endo, M. Furukawa, T. Mori, H. Ogasawara, J. Nakamura, *Angew. Chem. Int. Ed.* **2022**, e202212506.

[16] a) Y. Sun, C. Cao, P. Huang, S. Yang, W. Song, *RSC Adv.* **2015**, *5*, 86082–86087; b) C.-T. Hsieh, S.-h. Hsu, S. Maji, M. K. Chahal, J. Song, J. P. Hill, K. Ariga, L. K. Shrestha, *Mater. Horiz.* **2020**, *7*, 787–795; c) J. Song, T. Murata, K. C. Tsai, X. Jia, F. Sciortino, R. Ma, Y. Yamauchi, J. P. Hill, L. K. Shrestha, K. Ariga, *Adv. Mater. Interfaces* **2022**, *9*, 2102241.

[17] a) Y. Sun, C. Cao, P. Huang, S. Yang, W. Song, *RSC Adv.* **2015**, *5*, 86082–86087; b) Z. Tan, K. Ni, G. Chen, W. Zeng, Z. Tao, M. Ikram, Q. Zhang, H. Wang, L. Sun, X. Zhu, *Adv. Mater.* **2017**, *29*, 1603414.

[18] M. K. Rybarczyk, E. Gontarek, M. Lieder, M.-M. Titirici, *Appl. Surf. Sci.* **2018**, *435*, 543–551.

[19] a) Z.-l. Zhang, R. Brydson, Z. Aslam, S. Reddy, A. Brown, A. Westwood, B. Rand, *Carbon* **2011**, *49*, 5049–5063; b) P. J. Harris, *Crit. Rev. Solid State Mater. Sci.* **2005**, *30*, 235–253.

[20] D. Guo, R. Shibuya, C. Akiba, S. Saji, T. Kondo, J. Nakamura, *Science* **2016**, *351*, 361–365.

[21] C. Sundar, A. Bharathi, Y. Hariharan, J. Janaki, V. S. Sastry, T. Radhakrishnan, *Solid State Commun.* **1992**, *84*, 823–826.

[22] S. Zhang, Y. Wu, K. Luo, B. Liu, Y. Shu, Y. Zhang, L. Sun, Y. Gao, M. Ma, Z. Li, *Cell Rep. Phys. Sci.* **2021**, *2*, 100575.

[23] a) H. Li, W. Kang, L. Wang, Q. Yue, S. Xu, H. Wang, J. Liu, *Carbon* **2013**, *54*, 249–257; b) B. Ruiz-Camacho, J. Palafox-Segoviano, P. Pérez-Díaz, A. Medina-Ramírez, *Int. J. Hydrogen Energy* **2021**, *46*, 26027–26039; c) F.-X. Ma, J. Wang, F.-B. Wang, X.-H. Xia, *Chem. Commun.* **2015**, *51*, 1198–1201.

[24] a) C. Russo, B. Apicella, A. Ciajolo, *Energy Fuels* **2023**, *37*, 12525–12540; b) Y. Guo, Z. Ristovski, E. Graham, S. Stevanovic, P. Verma, M. Jafari, B. Miljevic, R. Brown, *Carbon* **2020**, *161*, 736–749.

[25] a) E. Groppo, F. Bonino, F. Cesano, A. Damin, M. Manzoli, in *Metal-free Functionalized Carbons in Catalysis: Synthesis, Characterization and Applications*, Royal Society of Chemistry,

2018, pp. 103–137; b) A. Sadezky, H. Muckenhuber, H. Grothe, R. Niessner, U. Pöschl, *Carbon* **2005**, *43*, 1731–1742.
[26] a) S. Liu, Y. Zhang, B. Ge, F. Zheng, N. Zhang, M. Zuo, Y. Yang, Q. Chen, *Adv. Mater.* **2021**, *33*, 2103133; b) A. C. Ferrari, J. Robertson, *Phys. Rev. B* **2000**, *61*, 14095.
[27] a) Y. Jia, L. Zhang, A. Du, G. Gao, J. Chen, X. Yan, C. L. Brown, X. Yao, *Adv. Mater.* **2016**, *28*, 9532–9538; b) X. Wang, Y. Jia, X. Mao, L. Zhang, D. Liu, L. Song, X. Yan, J. Chen, D. Yang, J. Zhou, *Chem* **2020**, *6*, 2009–2023.
[28] L. Yang, H. Liu, Z. Qiao, P. Sun, D. Li, R. Jiang, S. Liu, Z. Niu, Y. Zhang, T. Lin, *Adv. Energy Mater.* **2023**, 2204390.
[29] Y. Chen, J. Huang, Z. Chen, C. Shi, H. Yang, Y. Tang, Z. Cen, S. Liu, R. Fu, D. Wu, *Adv. Sci.* **2022**, *9*, 2103477.
[30] J. Zhu, Y. Huang, W. Mei, C. Zhao, C. Zhang, J. Zhang, I. S. Amiinu, S. Mu, *Angew. Chem. Int. Ed.* **2019**, *58*, 3859–3864.
[31] a) W. Ding, Z. Wei, S. Chen, X. Qi, T. Yang, J. Hu, D. Wang, L. J. Wan, S. F. Alvi, L. Li, *Angew. Chem. Int. Ed.* **2013**, *125*, 11971–11975; b) X. Wang, J. S. Lee, Q. Zhu, J. Liu, Y. Wang, S. Dai, *Chem. Mater.* **2010**, *22*, 2178–2180; c) C. Li, Z. Chen, A. Kong, Y. Ni, F. Kong, Y. Shan, *J. Mater. Chem. A* **2018**, *6*, 4145–4151.
[32] a) M. Pawlyta, J.-N. Rouzaud, S. Duber, *Carbon* **2015**, *84*, 479–490; b) G. Ye, S. Liu, K. Zhao, Z. He, *Angew. Chem. Int. Ed.* **2023**, *62*, e202303409.
[33] a) O. Marciano, S. Gonen, N. Levy, E. Teblum, R. Yemini, G. D. Nessim, S. Ruthstein, L. Elbaz, *Langmuir* **2016**, *32*, 11672–11680; b) D. Arčon, Z. Jagličič, A. Zorko, A. V. Rode, A. Christy, N. Madsen, E. G. Gamaly, B. Luther-Davies, *Phys. Rev. B* **2006**, *74*, 014438.
[34] a) K. Judai, S. Numao, A. Furuya, J. Nishijo, N. Nishi, *J. Am. Chem. Soc.* **2008**, *130*, 1142–1143; b) A. Manivannan, M. Chirila, N. Giles, M. Seehra, *Carbon* **1999**, *37*, 1741–1747.
[35] A. V. Rode, E. G. Gamaly, A. Christy, J. F. Gerald, S. Hyde, R. Elliman, B. Luther-Davies, A. Veinger, J. Androulakis, J. Giapintzakis, *Phys. Rev. B* **2004**, *70*, 054407.
[36] a) R. Zanasi, P. Fowler, *Chem. Phys. Lett.* **1995**, *238*, 270–280; b) J. Tuček, P. Błoński, J. Ugolotti, A. K. Swain, T. Enoki, R. Zbořil, *Chem. Soc. Rev.* **2018**, *47*, 3899–3990; c) T. Makarova, *Semiconductors* **2004**, *38*, 615–638.
[37] K. Bagani, M. K. Ray, B. Satpati, N. R. Ray, M. Sardar, S. Banerjee, *J. Phys. Chem. C* **2014**, *118*, 13254–13259.
[38] T. Shimizu, D. Lungerich, K. Harano, E. Nakamura, *J. Am. Chem. Soc.* **2022**, *144*, 9797–9805.
[39] a) A. V. Talyzin, S. Luzan, I. V. Anoshkin, A. G. Nasibulin, E. I. Kauppinnen, A. Dzwilewski, A. Kreta, J. Jamnik, A. Hassanien, A. Lundstedt, *J. Phys. Chem. C* **2014**, *118*, 6504–6513; b) R. M. Nikonova, N. S. Larionova, V. I. Lad'yanov, *Fullerenes Nanotubes Carbon Nanostruct.* **2022**, 1–13.
[40] a) K. Takeyasu, M. Furukawa, Y. Shimoyama, S. K. Singh, J. Nakamura, *Angew. Chem. Int. Ed.* **2021**, *60*, 5121–5124; b) K. Hayashida, R. Shimizu, Y. Hikita, K. Takeyasu, J. Nakamura, in *Electrochemical Society Meeting Abstracts 242*, The Electrochemical Society, Inc., **2022**, pp. 1599–1599.
[41] a) M. J. Frisch, G. W. Trucks, H. B. Schlegel, G. E. Scuseria, M. A. Robb, J. R. Cheeseman, G. Scalmani, V. Barone, G. A. Petersson, H. Nakatsuji, X. Li, M. Caricato, A. V. Marenich, J. Bloino, B. G. Janesko, R. Gomperts, B. Mennucci, H. P. Hratchian, J. V. Ortiz, A. F. Izmaylov, J. L. Sonnenberg, Williams, F. Ding, F. Lipparini, F. Egidi, J. Goings, B. Peng, A. Petrone, T. Henderson, D. Ranasinghe, V. G. Zakrzewski, J. Gao, N. Rega, G. Zheng, W. Liang, M. Hada, M. Ehara, K. Toyota, R. Fukuda, J. Hasegawa, M. Ishida, T. Nakajima, Y. Honda, O. Kitao, H. Nakai, T. Vreven, K. Throssell, J. A. Montgomery Jr., J. E. Peralta, F. Ogliaro, M. J. Bearpark, J. J. Heyd, E. N. Brothers, K. N. Kudin, V. N. Staroverov, T. A. Keith, R. Kobayashi, J. Normand, K. Raghavachari, A. P. Rendell, J. C. Burant, S. S. Iyengar, J. Tomasi, M. Cossi, J. M. Millam, M. Klene, C. Adamo, R. Cammi, J. W. Ochterski, R. L. Martin, K. Morokuma, O. Farkas, J. B. Foresman, D. J. Fox, Wallingford, CT, **2016**; b) J. D. Chai, M. Head-Gordon, *J. Chem. Phys.* **2008**, *128*; c) W. Wang, T. Sun, Y. Zhang, Y.-B. Wang, *J. Comput. Chem.* **2015**, *36*, 1763–1771; d) W. J. Hehre, R. Ditchfield, J. A. Pople, *J. Chem. Phys.* **1972**, *56*, 2257–2261; e) A. V. Marenich, C. J. Cramer, D. G. Truhlar, *J. Chem. Theory Comput.* **2009**, *5*, 2447–2464; f) R. Sander, *Atmos. Chem. Phys.* **2015**, *15*, 4399–4981; g) W. M. Haynes, 95th ed., CRC Press, Hoboken, **2014**; h) A. V. Marenich, J. M. Ho, M. L. Coote, C. J. Cramer, D. G. Truhlar, *Phys. Chem. Chem. Phys.* **2014**, *16*, 15068–15106; i) C. P. Kelly, C. J. Cramer, D. G. Truhlar, *J. Phys. Chem. B* **2007**, *111*, 408–422; j) A. J. Bard, R. Memming, B. Miller, *Pure Appl. Chem.* **1991**, *63*, 569–596.

Manuscript received: June 7, 2024
Accepted manuscript online: September 21, 2024
Version of record online: November 1, 2024